J. Fluid Mech. (2006), *vol.* 567, *pp.* 65–90.
doi:10.1017/S0022112006002084 Printed in the United Kingdom

Axisymmetric boundary integral simulations of film drainage between two viscous drops

By P. J. A. JANSSEN, P. D. ANDERSON, G. W. M. PETERS AND H. E. H. MEIJER

Materials Technology, Dutch Polymer Institute, Eindhoven University of Technology, P.O. Box 513, 5600 MB Eindhoven, The Netherlands
p.d.anderson@tue.nl

(Received 9 May 2005 and in revised form 6 April 2006)

Film drainage between two drops with viscosity equal to that of the matrix fluid is studied using a numerical method that can capture both the external problem of two touching drops and the inner problem of pressure-driven local film drainage, without assumptions about the dimensions of the film or the use of lubrication approximations. We use a non-singular boundary integral method that has sufficient stability and accuracy to simulate film thicknesses down to and smaller than 10^{-4} times the undeformed drop radius. After validation of the method we investigate the validity of various results obtained from simple film-drainage models and asymptotic theories. Our results for buoyancy-driven collisions are in agreement with a recently developed asymptotic theory. External-flow-driven collisions are different from buoyancy-driven collisions, which means that the internal circulation inside the drop plays a significant role in film drainage, even for small capillary numbers, as has been recently shown (Nemer *et al.*, *Phys. Rev. Lett.*, vol. 92, 2004, 114501). Despite that, we find excellent correspondence with simple drainage models when considering the drainage time only.

1. Introduction

Drop break-up and coalescence are the two main competing mechanisms in the microstructural evolution of blends that determine the final drop-size distribution and thus the final properties (see e.g. Tucker III & Moldenaers 2002 for a review). While break-up is a relatively well-understood phenomenon that is described quite well with various theories and numerical methods, as e.g. reviewed by Stone (1994), coalescence is much more complicated and there are still some unsolved problems.

Classically, coalescence is modelled as an outer problem of two touching spherical drops and an inner problem of pressure-driven film drainage. Coupling these two is complicated, since the dimensions of the film are many times smaller than the dimensions of the individual drops. Furthermore, coalescence is favoured by gentle collisions, where deformations are small, yet an accurate description of these deformations is vital. Therefore, most studies focus on film drainage between drops make assumptions about the coupling between the outer problem and the inner problem, and use asymptotic theories.

The inner problem is subdivided into three stages: approach, which can be considered as the motion of two freely and independently moving drops, film drainage, where the matrix fluid between the two drops is squeezed out, and film rupture, the point at which van der Waals forces rupture the film and coalescence occurs.

The film-drainage stage is the limiting step in this process, thus a thorough understanding of this phenomenon is necessary to calculate collision efficiencies, see for example Rother, Zinchenko & Davis (1997), Rother & Davis (2001), Bladwzdziewicz, Wajnryb & Loewenberg (1999). Analytical solutions for the drainage between flat interfaces with various mobilities have been reviewed by Chesters (1991).

When assuming small deformations, film drainage can be described by an asymptotic theory, yielding a set of coupled integro-differential equations. Two typical assumptions concerning the coupling of the global problem to the local problem are the cases of constant approach force and constant approach velocity. Yiantsios & Davis (1990, 1991) made an important step for thin-film descriptions by coupling the velocity of the surface and the tangential stress acting upon the surface via a local boundary integral method. Examples of numerical studies on the local film drainage are numerous, and often include the effects of surfactants (see e.g. Li 1994, Rother *et al.* 1997; Bazhlekov, Chesters & van de Vosse 2000; Chesters & Bazhlekov 2000; Valkovska, Danov & Ivanov 2000; Yeo *et al.* 2003). What is lacking in the literature is a justification of the validity of the assumptions and couplings made. It is generally assumed that the external velocity does not play a role in film drainage for small capillary numbers. However, it has been shown recently that the external flow can halt the drainage (Cristini, Blawzdziewicz & Loewenberg 2001; Nemer *et al.* 2004). Besides showing this effect, these authors also provided a theory which incorporates the onset of a stationary state for drops in a flow-driven head-on collision, and gave an accurate prediction of the stationary film thickness, validated with boundary integral simulations.

Boundary integral methods are typically used to simulate the approach stage, and are considered to provide the exact solution of the flow problem for Newtonian, inertialess drops. Stability and accuracy requirements become stricter for drops in close approach and at small capillary numbers, which limits the use of these methods, as they fail at relative large film thicknesses and relative large capillary numbers (Rother *et al.* 1997). More complex algorithms are required with an extremely fine discretization of the interface (Zinchenko & Davis 2005). In contrast to this, a non-singular boundary integral method is considerably more accurate and stable and thus more suited to study film drainage (Bazhlekov, Anderson & Meijer 2004).

The objective of this work is to investigate the film-drainage process as function of the capillary number and the drop radius, while maintaining a full drop description; the influence of the viscosity ratio between drop and matrix fluid is not studied. In particular we are interested in comparing numerical results with asymptotic theories and investigate the validity of the assumptions made therein. Furthermore, we address some questions that were raised recently after a series of experiments (Leal 2004).

This paper is organized as following. First, in § 2 the formulation of the flow problem is presented. Next, the method to solve the resulting equations is discussed in § 3. Using a full drop description, the validity of various results from asymptotic theories is tested, and subsequently the drainage time of head-on collisions between two viscous drops is investigated. The results are compared to recently published experimental data, obtained in a four-roll mill, see § 4. Finally, conclusions are drawn in § 5.

2. Mathematical formulation

Drops with deformable interfaces subjected to an external flow or an external force are considered. Both the drop phase and matrix fluid are Newtonian and incompressible and, since highly viscous drops are considered, inertia terms are neglected.

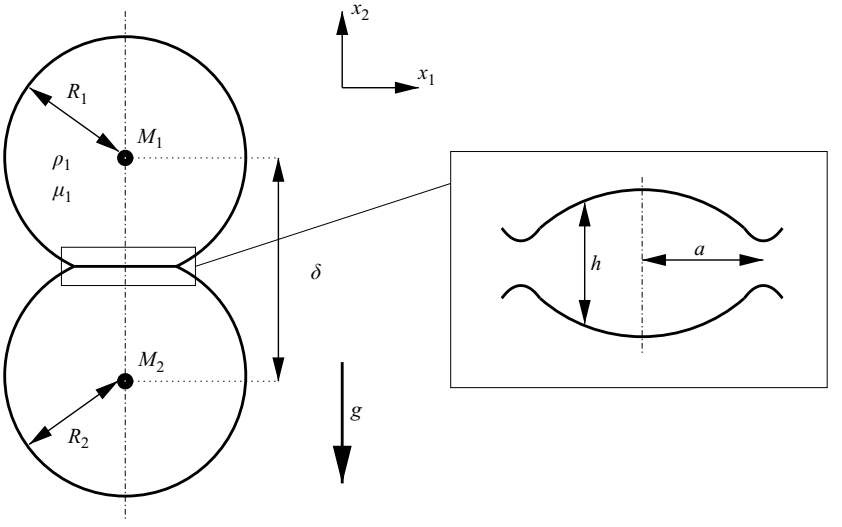

FIGURE 1. Schematic representation of two coalescing drops in a matrix fluid with density $\rho_0 = \rho$; $\rho_1 = \rho + \Delta\rho$, viscosity $\mu_0 = \mu$; $\mu_1 = \lambda\mu$.

This reduces the problem to Stokes flow. The governing equations for the full domain of each phase are:

$$\left.\begin{aligned} -\nabla p_i + \mu_i \nabla^2 \boldsymbol{u}_i + \rho_i \boldsymbol{g} &= \boldsymbol{0}, \\ \nabla \cdot \boldsymbol{u}_i &= 0, \end{aligned}\right\} \quad i = 0, 1, 2, \tag{2.1}$$

where p is the pressure, μ the viscosity, ρ the density and $\boldsymbol{u}$ the velocity. The index i refers to different phases, where the matrix phase is indicated by $i = 0$, see also figure 1. The buoyancy term $\rho_i \boldsymbol{g}$ in equation (2.1) acts as a body force. Buoyancy effects are considered since they give an opportunity to move drops without the need of an external flow. If an external flow is considered, the velocity at infinity is prescribed:

$$\boldsymbol{u}_\infty(\boldsymbol{x}) = G\boldsymbol{L} \cdot \boldsymbol{x}, \tag{2.2}$$

where G represents the strength of the flow and $\boldsymbol{L}$ is a tensor which describes the flow type. For both cases, the boundary conditions at the matrix–drop interface are continuity of velocity,

$$\boldsymbol{u}_0(\boldsymbol{x}) = \boldsymbol{u}_i(\boldsymbol{x}), \tag{2.3}$$

and the stress balance,

$$(\boldsymbol{\Pi}_0(\boldsymbol{x}) - \boldsymbol{\Pi}_i(\boldsymbol{x})) \cdot \boldsymbol{n}(\boldsymbol{x}) = \boldsymbol{f}(\boldsymbol{x}). \tag{2.4}$$

The stress tensor in the ith fluid can be written as

$$\boldsymbol{\Pi}_i = -p_i \boldsymbol{I} + \mu_i (\nabla \boldsymbol{u}_i + (\nabla \boldsymbol{u}_i)^c), \tag{2.5}$$

with $\boldsymbol{I}$ the unit tensor. The vector $\boldsymbol{f}$ in equation (2.4) represents the jump in stress across the interface. The interfacial forces considered here are the capillary pressure and the disjoining pressure. The buoyancy term in equation (2.1) can also be expressed as an interfacial force, since this term can be considered as an additional hydrostatic pressure, correcting the pressure in the ith fluid by the term $-\rho_i(\boldsymbol{g} \cdot \boldsymbol{x})$. So finally $\boldsymbol{f}$

becomes

$$\boldsymbol{f}(\boldsymbol{x}) = \left(2\sigma\kappa(\boldsymbol{x}) - \frac{H}{6\pi h^3(\boldsymbol{x})} \pm \Delta\rho(\boldsymbol{g}\cdot\boldsymbol{x})\right)\boldsymbol{n}(\boldsymbol{x}), \tag{2.6}$$

where σ is the interfacial tension, κ the local curvature, H the effective Hamaker constant, h the local minimum distance to the other interface, and $\Delta\rho$ the absolute density difference between the drop and the matrix phase. The curvature κ is defined as $\kappa(\boldsymbol{x}) = \nabla_s \cdot \boldsymbol{n}(\boldsymbol{x})$, with $\nabla_s = (\boldsymbol{I} - \boldsymbol{nn})\cdot\nabla$ the surface gradient operator. Finally, the kinematic condition at the interface is

$$\frac{\mathrm{d}\boldsymbol{x}}{\mathrm{d}t} = \boldsymbol{u}(\boldsymbol{x}, t). \tag{2.7}$$

We use the boundary integral method (BIM) to calculate the velocity. Since we consider the limit of Stokes flow for two Newtonian fluids, the velocity only depends on the location of the interfaces, and, therefore, this method is applicable. That only the interface needs to be described is also the main advantage of the BIM; thus the method allows a detailed resolution of the film with limited computational effort. The BIM gives the velocity at any point $\boldsymbol{x}_0$ on the surface S as (Rallison & Acrivos 1978; Pozrikidis 1992):

$$\begin{aligned}(\lambda+1)\boldsymbol{u}(\boldsymbol{x}_0) = 2\boldsymbol{u}_\infty(\boldsymbol{x}_0) &- \frac{1}{4\pi\mu_i}\int_S \boldsymbol{G}(\boldsymbol{x}_0, \boldsymbol{x})\cdot\boldsymbol{f}(\boldsymbol{x})\,\mathrm{d}S(\boldsymbol{x}) \\ &- \frac{\lambda-1}{4\pi}\int_S \boldsymbol{u}(\boldsymbol{x})\cdot\boldsymbol{T}(\boldsymbol{x}, \boldsymbol{x}_0)\cdot\boldsymbol{n}(\boldsymbol{x})\,\mathrm{d}S(\boldsymbol{x}),\end{aligned} \tag{2.8}$$

where S includes all surfaces. In this equation $\boldsymbol{G}$ represents the Stokeslet, also known as the single-layer potential, and $\boldsymbol{T}$ the stresslet, also known as the double-layer potential. Only flows in unbounded regimes (no walls or solid objects in the domain) are considered in this work. In that case the free-space kernels are defined as

$$\left.\begin{aligned}\boldsymbol{G}(\boldsymbol{x}_0, \boldsymbol{x}) = \boldsymbol{G}(\hat{\boldsymbol{x}}) &= \frac{\boldsymbol{I}}{|\hat{\boldsymbol{x}}|} + \frac{\hat{\boldsymbol{x}}\hat{\boldsymbol{x}}}{|\hat{\boldsymbol{x}}|^3}, \\ \boldsymbol{T}(\boldsymbol{x}, \boldsymbol{x}_0) = \boldsymbol{T}(\hat{\boldsymbol{x}}) &= -6\frac{\hat{\boldsymbol{x}}\hat{\boldsymbol{x}}\hat{\boldsymbol{x}}}{|\hat{\boldsymbol{x}}|^5},\end{aligned}\right\} \tag{2.9}$$

with $\hat{\boldsymbol{x}} = \boldsymbol{x} - \boldsymbol{x}_0$.

2.1. *Dimensionless equations*

Often it is convenient to recast equations into their non-dimensional form, since that facilitates a comparison between different situations. Two different scalings are introduced: one for external-flow and one for buoyancy-driven coalescence.

For the external flow case the following dimensionless parameters are introduced:

$$u = u^* RG, \quad p = p^*\frac{\sigma}{R}, \quad \mu_i = \lambda^*\mu_0, \quad \nabla = \frac{\nabla^*}{R}, \quad \kappa = \frac{\kappa^*}{R}, \quad h = h^* R, \quad t = \frac{t^*}{G}, \tag{2.10}$$

where * indicates a dimensionless parameter. R is the undeformed drop radius (we will assume here for simplicity only equal-sized drops, so there is no need to introduce an equivalent drop radius), G is the shear or elongational rate, λ is the viscosity ratio between the drop and matrix phases. In addition to h all other lengths are scaled with R. We will only consider equal viscosities, so $\lambda = 1$, in which case the term in front of the second integral on the right-hand side of equation (2.8) vanishes, and the unknown velocity $\boldsymbol{u}$ is no longer found on the right-hand side, thus eliminating the need for a matrix inversion or an iterative procedure. Other difficulties when

simulating cases with $\lambda \neq 1$ include the need for highly efficient solvers (Zinchenko, Rother & Davis 1997) and an extreme influence of global errors on the solution in the whole domain, particularly in the film (Bazhlekov *et al.* 2004).

In what follows only dimensionless parameters are considered (unless stated otherwise), and the index * is dropped. The BIM formulation becomes

$$\boldsymbol{u}(\boldsymbol{x}_0) = \boldsymbol{u}_\infty(\boldsymbol{x}_0) - \frac{1}{8\pi}\int_S \mathbf{G}(\boldsymbol{x}_0, \boldsymbol{x})\cdot \boldsymbol{f}(\boldsymbol{x})\,\mathrm{d}S(\boldsymbol{x}), \tag{2.11}$$

and the stress jump in dimensionless form is

$$\boldsymbol{f}(\boldsymbol{x}) = \frac{1}{Ca}\left(2\kappa(\boldsymbol{x}) - \frac{A}{h^3(\boldsymbol{x})}\right)\boldsymbol{n}(\boldsymbol{x}), \tag{2.12}$$

in which the two dimensionless parameters Ca and A appear. Ca is the capillary number, the ratio between the viscous forces and the interfacial forces, and A is the dimensionless Hamaker parameter:

$$Ca = \frac{RG\mu}{\sigma}, \qquad A = \frac{H}{6\pi\sigma R^2}. \tag{2.13}$$

Since $\lambda = 1$, equation (2.11) is valid for the whole domain, not just for the drop surface (Pozrikidis 1992).

In the buoyancy case the same scaling as for external-driven collisions is used (see equation (2.10)), except for a different characteristic velocity and time scale:

$$u = u^*\frac{\Delta\rho R^2 g}{\mu}, \quad t = t^*\frac{\mu}{\Delta\rho R g}, \tag{2.14}$$

where g is the gravitational acceleration. The dimensionless form of the stress jump in this case becomes

$$\boldsymbol{f}(\boldsymbol{x}) = \left[\frac{1}{Bo}\left(2\kappa(\boldsymbol{x}) - \frac{A}{h^3(\boldsymbol{x})}\right) \pm x_2\right]\boldsymbol{n}(\boldsymbol{x}), \tag{2.15}$$

where Bo is the Bond number, defined as

$$Bo = \frac{\Delta\rho g R^2}{\sigma}. \tag{2.16}$$

The additional term in equation (2.15), x_2, is the local x_2-coordinate scaled with R; the gravity is considered parallel to the x_2-axis and the sign is determined by whether the drop rises or sinks due to the density difference. We also define the film radius a and the distance between the centres of mass of the two drops δ, as can be seen in figure 1. Both a and δ are scaled with R.

In most thin-film simulations different scalings based on the film radius are used. Since in this paper we often compare our results to those of thin-film simulations, these scaling relationships are also given here. The dimensionless parameters are indicated with a bar:

$$\bar{h} = \frac{hR}{2a^2}, \quad \bar{t} = \frac{2t\sigma a}{\mu R^2}, \quad \bar{A} = \frac{HR^4}{4\pi\sigma a^6}. \tag{2.17}$$

In the dimensionless variables used here this becomes

$$\bar{h} = \frac{h^*}{2a^{*2}}, \quad \bar{t}_{buo} = \frac{2t^*a^*}{Bo}, \quad \bar{t}_{ext} = \frac{2t^*a^*}{Ca}, \quad \bar{A} = \frac{3A}{2a^{*6}}. \tag{2.18}$$

The subscript *buo* refers to buoyancy-driven collisions, *ext* refers to external-flow-driven collisions.

3. Numerical scheme

Since only head-on collisions are studied, an axisymmetric framework can be used, and in this case an analytical azimuthal integration is combined with surface integrals, that reduce to line integrals over an arclength s. The last are calculated by summing over N line segments. We use the non-singular contour-integral representation of Bazhlekov *et al.* (2004). For the axisymmetric case, the contribution of a surface part s_j, between $\boldsymbol{x}_j$ and $\boldsymbol{x}_{j+1}$, with constant $\boldsymbol{f}$ is (see Bazhlekova & Bazhlekov 2003)

$$\int_{s_j} f_n(\boldsymbol{x})\mathbf{G}(\hat{x})\cdot\boldsymbol{n}(\boldsymbol{x})\,\mathrm{d}s(\boldsymbol{x}) = f_n(\boldsymbol{I}^G(\boldsymbol{x}_0, \boldsymbol{x}_{j+1}) - \boldsymbol{I}^G(\boldsymbol{x}_0, \boldsymbol{x}_j)), \tag{3.1}$$

where

$$f_n = \boldsymbol{f}\cdot\boldsymbol{n} \tag{3.2}$$

and $\boldsymbol{I}^G(\boldsymbol{x}_0, \boldsymbol{x}_j)$ is the integration over the circle that makes up the contour of the surface in three-dimensional space, and can be expressed in complete elliptic integrals of the first and second kind. These elliptic integrals are calculated using polynomials of Abramowitz & Stegun (1965). Equation (3.1) can be rewritten to give the contribution over a line segment between two nodes as

$$\int_{s_j} f_n(\boldsymbol{x})\mathbf{G}(\hat{\boldsymbol{x}})\cdot\boldsymbol{n}(\boldsymbol{x})\,\mathrm{d}s(\boldsymbol{x}) = (f_n(\boldsymbol{x}_j) - f_n(\boldsymbol{x}_{j+1}))\boldsymbol{I}_j^G, \tag{3.3}$$

with $\boldsymbol{I}_j^G$ evaluated in the middle of the line segment. This leads to a formulation where only gradients in $\boldsymbol{f}$ are taken into account, similar to the three-dimensional case.

The curvature and normal vector are calculated using the local parabola fitting method of Davis (1999). This proved to be a quick and stable method, especially for non-uniform meshes. Notice that the normal vector does not enter the boundary-integral calculation, but is used to split the velocity into a normal and a tangential part, motivation for which is given below.

For the time integration a multiple time-step method is used. The kernel calculation, which is the most expensive part in terms of computational time, is performed only every M steps, while all other parameters are calculated at every time step (Bazhlekov *et al.* 2004). Here $M = 100$ in all simulations. Time integration during a small time-step was performed with a second-order Runge–Kutta method. Although the multi-step scheme provides stability, the time-step required for accuracy is smaller, especially with decreasing film thickness. In all cases the time step was made proportional to the capillary number (or Bond number in case of a buoyancy-driven collision) and to the square root of the minimal film thickness: $\Delta t \propto Cah_{min}^{1/2}$, with an upper limit of 10^{-5} to ensure stability and a lower limit of 10^{-9} to keep computational time within limits. The proportionality factor was in the order of 10^{-3}.

The hydrodynamical velocity is split into two parts: a normal and a tangential component:

$$\left.\begin{aligned}\boldsymbol{u}_n &= u_n\boldsymbol{n} = (\boldsymbol{u}\cdot\boldsymbol{n})\boldsymbol{n},\\ \boldsymbol{u}_t &= u_t\boldsymbol{t} = (\boldsymbol{u}\cdot\boldsymbol{t})\boldsymbol{t},\end{aligned}\right\} \tag{3.4}$$

where $\boldsymbol{t}$ is the vector tangential to the interface. The position of the interface is updated with the normal part of the hydrodynamical velocity and an additional

Nodes	h_{min} at $t = 1.93$	Rel. error	h_{min} at $t = 10$	Rel. error
100	1.5225×10^{-4}	0.574	8.8321×10^{-5}	0.0139
200	2.5873×10^{-4}	0.276	8.7664×10^{-5}	0.00639
400	3.2288×10^{-4}	0.097	8.7302×10^{-5}	0.00224
800	3.5760×10^{-4}	—	8.710×10^{-5}	—

TABLE 1. Convergence of the minimal film thickness at two moments in time. The relative error is based on the 800 node result.

term:

$$\frac{\mathrm{d}\boldsymbol{x}}{\mathrm{d}t} = \boldsymbol{u}_n(\boldsymbol{x}, t) + \boldsymbol{v}(\boldsymbol{x}, t). \tag{3.5}$$

The additional velocity in equation (3.5), $\boldsymbol{v}(\boldsymbol{x}, t)$, is tangential to the interface and thus will not influence the solution. It is only used for nodal redistribution to keep the mesh in good shape and move nodes to locations where a finer discretization is required. For this we used a method similar to the one proposed by Loewenberg & Hinch (1996). Nodes are only convected to the minimal film thickness position; the distance between nodes is independent of the local curvature. To ensure a smooth distribution of the nodes (which is advantageous for the curvature calculation), the minimal thickness inserted in the distribution function is the minimum of the local node and the 10 nodes surrounding it (five on each side). Furthermore, the distance between the nodes far away from the film is kept constant. Finally, since only equal-sized drops are considered, all calculations are done for one drop only and then mirrored around $z = 0$. Notice that the BIM calculations involve integration over both surfaces.

One additional note on post-processing is pertinent. Due to the discrete nature of the position of nodes and the additional tangential velocity, the film radius and minimal film thickness can make step-wise position changes in time and, more notably, the actual location of the minimal film thickness probably does not coincide with the location of a node. To solve this problem, the minimal film thickness and film radius were determined using higher-order approximations where, using the normal vector and the curvature, a circle was fitted through the node where the film thickness was minimal; the same was done for the two surrounding nodes. The line between two nodes was projected on a linear combination of the two fitted circles, see Bazhlekov *et al.* (2004) for a more detailed description. This higher-order projection was not used to get a better estimate for the minimal film thickness when calculating the disjoining pressure.

To show that the boundary integral method described in this section is suitable to describe the small interfacial distances, we present the evolution of the minimal film thickness in time for an external-flow-driven collision with $Ca = 0.005$ for simulations done with 100, 200, 400 and 800 nodes per drop, see figure 2. The results converge and provide a stable solution for h_{min}, even below 10^{-4}. In table 1 the values of h_{min} for the varying number of nodes are given at two moments in time. Also, the error relative in the result for 800 nodes is given. Clearly, 100 nodes per drop are insufficient, but for 200 and more, the differences appear to be reasonable to good. The greatest errors relative to the 800 node simulation are at $t \approx 1.9$. At this moment the film is formed. However, as the simulations continue, the results all convergence, showing that a relatively crude discretization (relative to the film thickness) is sufficient to give consistent results. This is demonstrated in the inset of figure 2, where the film profile

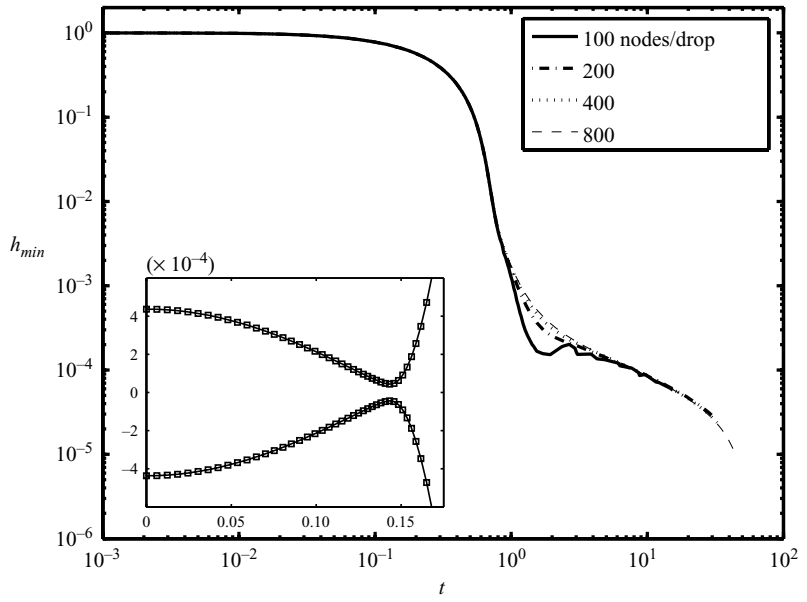

FIGURE 2. Evolution of the minimal film thickness over time for $Ca = 0.005$; simulations are conducted with a varying number of nodes per drop. The inset shows the film profile for the 400 nodes case at $t = 10$, where the squares indicate the location of the nodes.

at $t = 10$ for the 400 node simulation is shown. The minimal nodal distance is of the order of 10^{-3}, while the film thickness is below 10^{-4}.

4. Results and discussion

We first compare our results for buoyancy-driven (quiescent) head-on collisions of initially spherical drops with an asymptotic theory. Subsequently external-flow-driven collisions are studied, with and without van der Waals forces included. Finally, we compare our data for the drainage time with experimental data and those of a simple drainage model. The initial separation between the centres of mass of the drops, denoted by δ, is either $3R$ or $4R$. For the external-flow-driven collisions we use a bi-axial extensional flow, so the prescribed velocity in scaled, axisymmetric coordinates is

$$\boldsymbol{u}_\infty(\boldsymbol{x}) = \left(\tfrac{1}{2}r, -z\right)^T. \tag{4.1}$$

4.1. *Buoyancy-driven collisions*

First we consider gravity-driven collisions, which can be considered as a constant approach force case. We take as an example a rather academic situation of two approaching drops, one rising and one sinking. Due to the long time scales involved, the simulation is conducted with 200 nodes per drop only, thus limiting the computational time. The Bond number was set to 0.0653 (corresponding with $r_\infty/a = 0.417$ in Nemer (2003)) for both drops and simulations were started with an initial distance between the drops of $\delta = 3R$. Instead of showing film shapes at multiple times, we prefer to present the evolution of three most relevant parameters in time: the film thickness at the centreline h_{cent}, the minimal film thickness h_{min} and the film radius a, since this provides quantitative measures concerning their evolution. The evolution of the film radius is shown in figure 3. Initially the film radius is 0, i.e. the drops

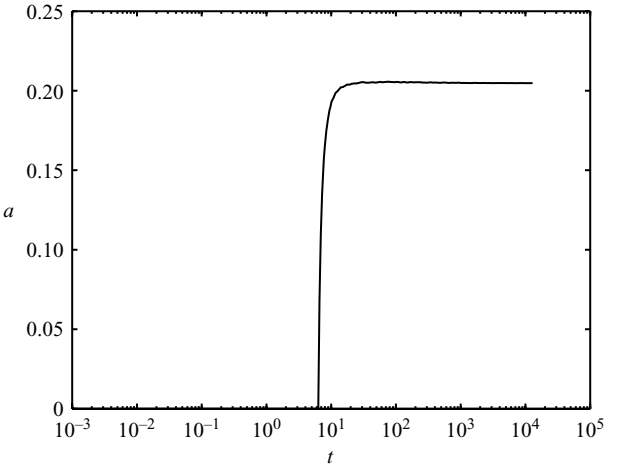

FIGURE 3. Film radius over time for a buoyancy-driven collision with $Bo = 0.0653$.

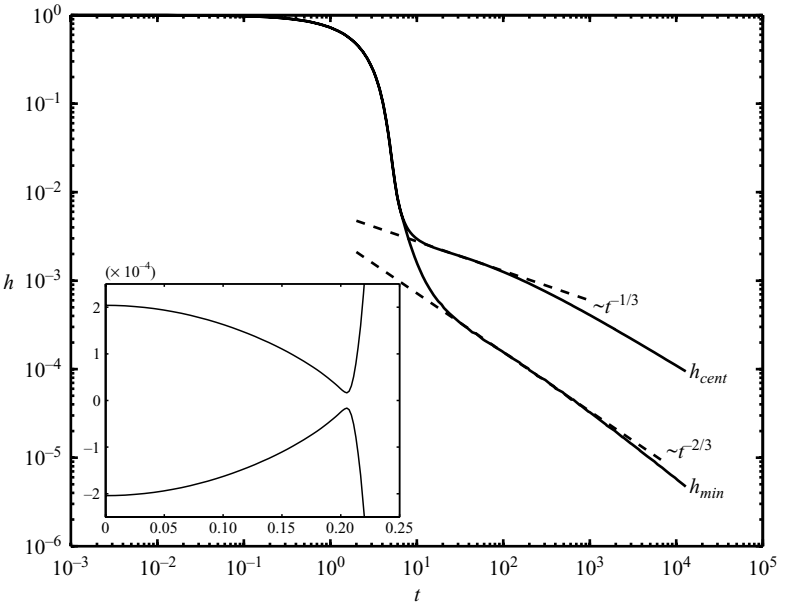

FIGURE 4. Minimal film thickness over time and film thickness at the centreline for $Bo = 0.0653$. The solid lines represent the current results, the dashed lines the partly mobile asymptotes of Yiantsios & Davis (1990). The inset shows the film profile at $t = 1000$.

are still spherical. As the drops approach, the film starts to form, reaching a steady value in a relatively short time. Small-deformation theory predicts a film radius of $a = 0.816Bo^{1/2}$, which yields $a = 0.21$ for $Bo = 0.0653$ which corresponds excellent to our simulation. The evolutions of h_{min} and h_{cent}, figure 4, initially show a fast decrease. After the film is formed, both thicknesses follow a trend that is similar to the asymptotes found by the thin-film description of Yiantsios & Davis (1990): $h_{cent} \sim t^{-1/3}$ and $h_{min} \sim t^{-2/3}$, based on a scaling argument of Jones & Wilson (1978). For the case of constant approach force this behaviour for the minimal film thickness

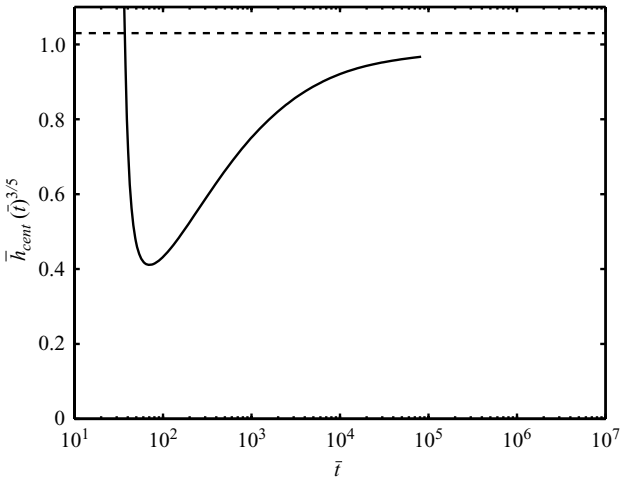

FIGURE 5. Rescaled centreline film thickness as a function of rescaled time. The dashed line is the asymptote of Nemer (2003).

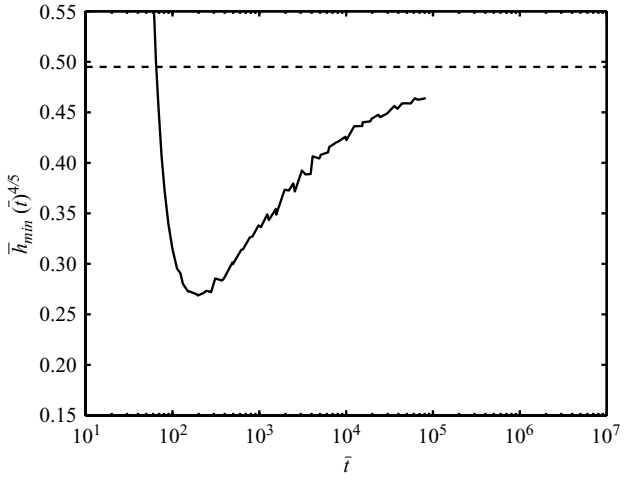

FIGURE 6. Rescaled minimum film thickness as a function of rescaled time. The dashed line is the asymptote of Nemer (2003).

was later generalized for low viscosity ratios by Bazhlekov *et al.* (2000). These trends are not reached in our simulation until $h < 10^{-3}R$, the limit where most current full drop methods fail.

However, continuing the simulations over prolonged time spans, the results start to diverge from the asymptotes of Yiantsios & Davis (1990), so their scaling only seems to happen to fit the drainage behaviour over some intermediate regime. Nemer (2003) derived an analytical solution for the constant approach case, with the long-term asymptotes $\bar{h}_{min} = 0.495(\bar{t})^{-4/5}$ and $\bar{h}_{cent} = 1.03(\bar{t})^{-3/5}$. Thin-film simulations supported these findings, with only minor differences in the absolute value. If we plot $\bar{h}_{cent}(\bar{t})^{3/5}$ and $\bar{h}_{min}(\bar{t})^{4/5}$ versus $\bar{t}$, see figures 5 and 6, the results indicate that these variables seem to become constant, verifying the asymptotes, indicated with the dashed lines. There is also a good match with the absolute value, but slightly off, similar to the results of

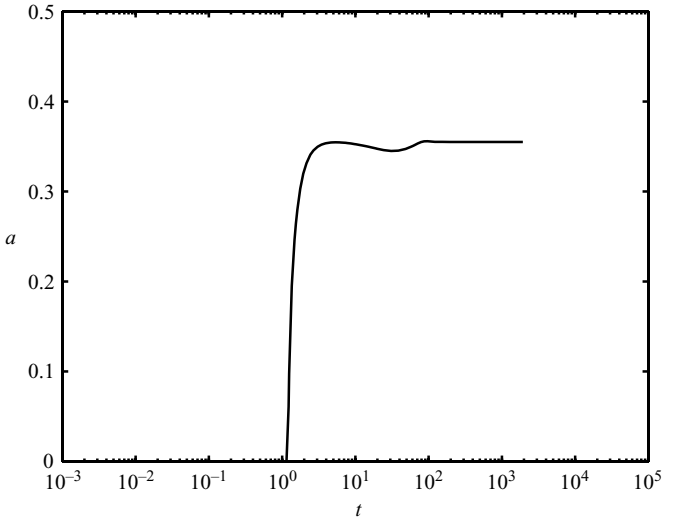

FIGURE 7. Film radius over time for an external-flow-driven collision with $Ca = 0.04$.

Nemer (2003). A final verification of these asymptotes requires much longer computations, which, given the logarithmic time axes, we were not able to conduct (the current simulations took approximately four weeks on an AMD Athlon 64 3400+ processor).

The noise in figure 6 is due to the use of 200 nodes only. More nodes would provide a smoother solution, but it is expected that the overall trend will remain the same.

4.2. *External-flow-driven collisions*

Next, external-flow-driven collisions are considered, since they are the most relevant for practical applications. The initial drop separation δ is again $3R$ and simulations are conducted with 400 nodes per drop. The evolution of the film radius is shown in figure 7 for $Ca = 0.04$, and a similar evolution as for the buoyancy-driven case is found: the film radius reaches a steady value in a relatively short time. There is a temporary decrease, after which the film radius once again attains the same constant value as before. This temporary decrease is not a computational artifact, and will be discussed below. The overall trend is that the film radius is constant, which corresponds to a constant approach force case, while for a constant approach velocity the film radius evolves as $a \sim \sqrt{t}$ (Abid & Chesters 1994; Klaseboer *et al.* 2000; Yeo *et al.* 2003).

Comparing the final value of the film radius for different capillary numbers, we find that the film radius scales as $Ca^{1/2}$, see figure 8. This is a common result of film drainage theories. Even the absolute value gives excellent correspondence with the prediction of small deformation theory ($a = 2.086Ca^{1/2}$). For high capillary numbers the film radius is slightly smaller, since small deformation theory loses its validity here. At the lowest capillary numbers we also see a deviation, which we contribute to the discretization, i.e. the film is only described with a few nodes (the film radius is of the order of Δs).

It was found by Cristini *et al.* (2001), and discussed in more detail by Nemer *et al.* (2004), that the internal circulation inside the drop will eventually halt film drainage. We compare our results to theirs and then investigate this phenomenon in more detail. First we plot the evolution of the minimal and centreline film thickness, see figures 9 and 10, for $Ca = 0.1$ and 0.04 respectively. In all cases we find an initial decrease in

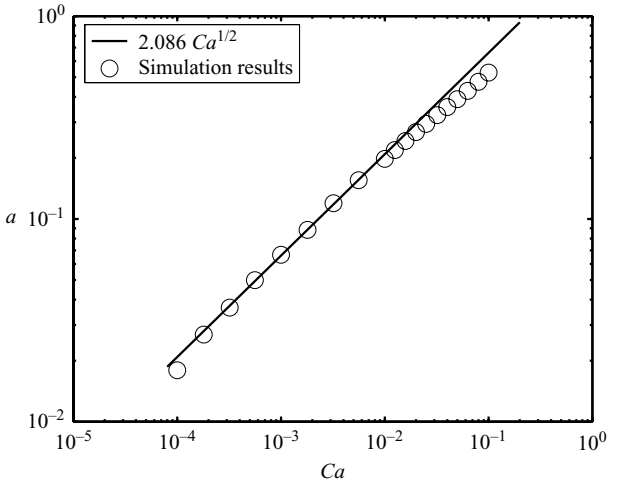

FIGURE 8. Steady film radius in an external-flow-driven collision for multiple capillary numbers. The symbols are the results of our simulations. The solid line is the prediction of small-deformation theory.

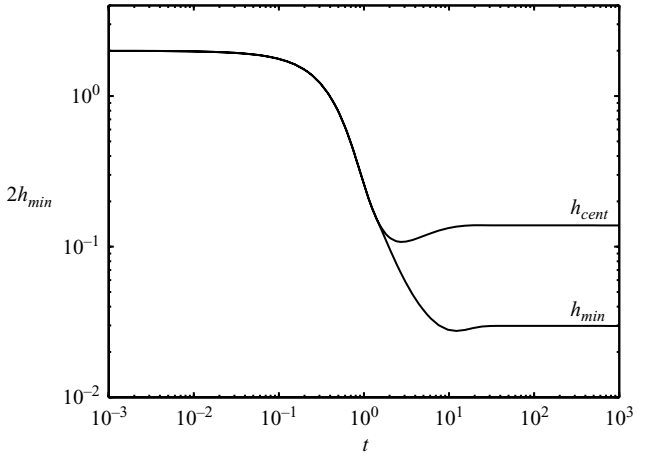

FIGURE 9. Minimal and centreline film thickness over time in an external-flow-driven collision for $Ca = 0.1$.

film thickness, then a minimum, followed by an increase again to arrive, after a small overshoot, at a steady value. In Nemer *et al.* (2004) all length scales are scaled with $R/2$, so our values would correspond to $\hat{G} = 0.05$ and $\hat{G} = 0.02$. We converted our data to this scaling to allow a direct comparison with their figure 1.

According to Nemer *et al.* (2004), the steady-state film thickness as function of the capillary number scales as $h_{cent} = 2.43Ca^{3/2}$ and $h_{min} = 11.3Ca^3$. These relationships are reproduced in figure 11 for multiple capillary numbers together with our results. For the steady value of h_{min} we have plotted results of simulations where a steady state minimum was obtained (for the lower capillary numbers, $Ca < 3.10^{-2}$, we could not fully obtain the long-term behaviour, limited by computation time). Figure 11 shows that again we obtain an excellent match with the results of Nemer *et al.* (2004). Similar to these authors, we also find that the theory underestimates the stationary value of

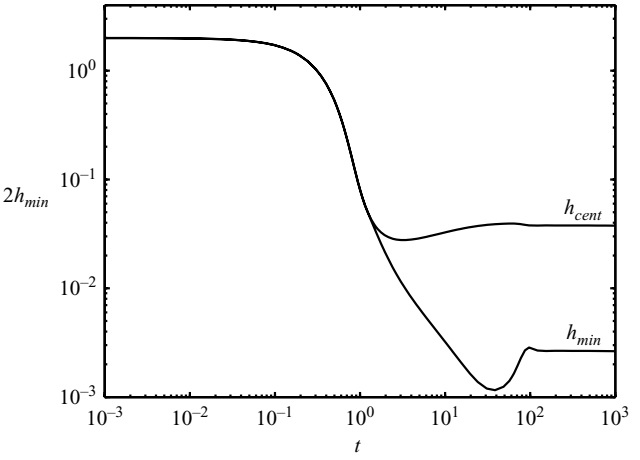

FIGURE 10. As figure 9, but for $Ca = 0.04$.

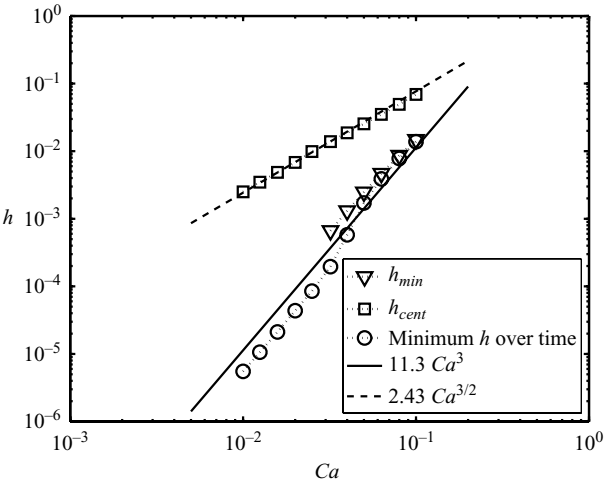

FIGURE 11. The stationary end values of the minimal and centreline film thickness. Also shown is the minimum h_{min} obtained over time and the two predictions from Nemer *et al.* (2004).

h_{min} by a factor 2. Also shown in figure 11 is the minimum value obtained over time of h_{min}, and it is seen that for high capillary numbers the difference between the temporal minimum and the steady-state minimal film thickness is relatively small. However, starting from $Ca = 0.04$ downwards the temporal minimum becomes significantly lower, and eventually scales as Ca^3 again. This temporal minimum will be discussed in § 4.3 when van der Waals forces are taken into consideration.

As was shown in figure 7 the film radius is not constant in time. Once film drainage is halted, the radius decreases, followed by an increase to the previous value which corresponds to the prediction of the small deformation theory. Also h_{min} and h_{cent} reach minima before approaching their final stationary values. To illustrate this in more detail, film profiles are shown at three different times in figure 12: at $t = 12$, which corresponds to a time when h_{min} equals the stationary film thickness before the minimum is obtained; at $t = 38$, when the minimum in time is obtained; and $t = 1200$

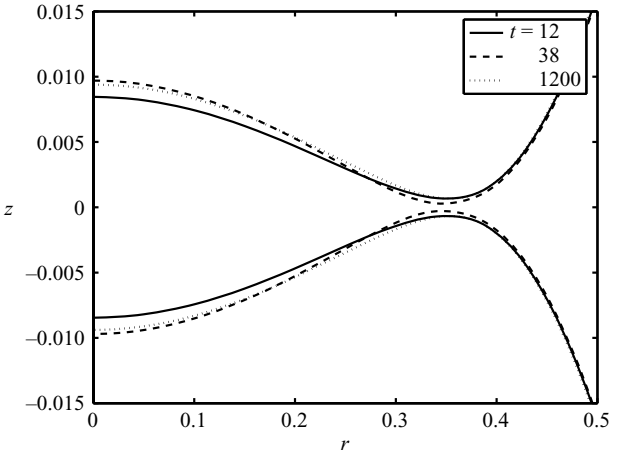

FIGURE 12. The film profile for $Ca = 0.04$ at three moments in time.

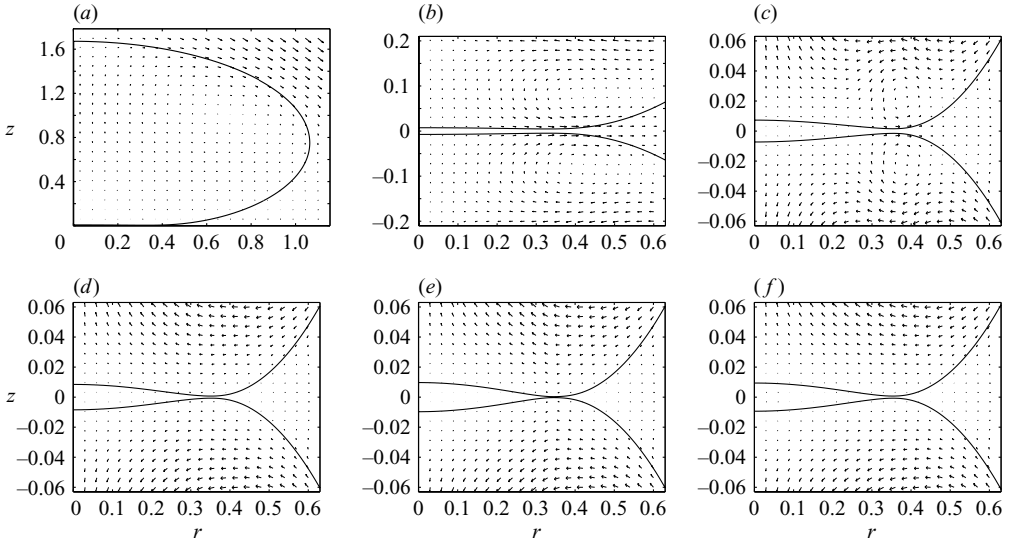

FIGURE 13. Velocity field in and around the drop for $Ca = 0.04$. (*a*) $t = 2$ (showing the macroscopic vortex inside the drop). (*b*) $t = 2$ (plotting the film profile). (*c*) $t = 5$ (with rescaled vertical axis). (*d*) $t = 12$ ($h_{min} = h_{min,stat}$). (*e*) $t = 38$ (minimum h_{min} in time is obtained here). (*f*) $t = 1200$ (long-term steady state).

where the film profile is stable. We observe that the film volume in the steady-state situation is larger than at $t = 12$, i.e. matrix fluid was dragged into the film in this period. One other observation is that the rim is relatively flat compared to the film profile we find in buoyancy-driven collisions (see the inset of figure 4).

To understand what is happening in the film as film drainage is halted, we show velocity fields inside and outside the drops in figure 13. The external flow generates a large vortex inside the drop (figure 13*a*), which remains present at all times. The pressure-driven outflow is initially sufficiently strong to overcome the internal vortex inside the drop and forms a small counter-rotating vortex above the film (figure 13*b*), and shrinking in size over time (figure 13*c*). Eventually this vortex disappears altogether

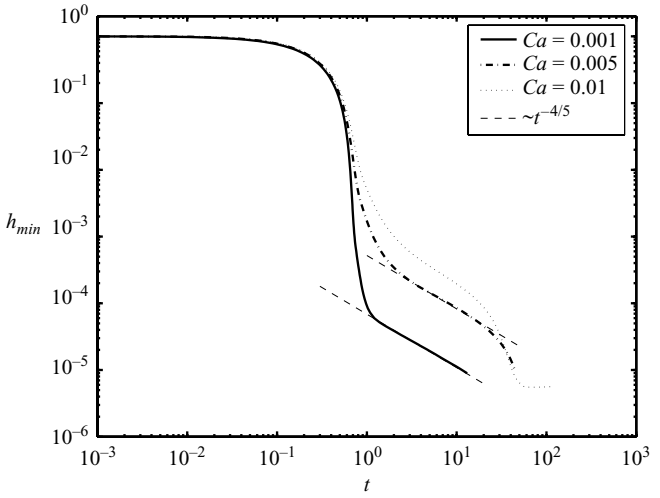

FIGURE 14. Minimal film thickness over time for multiple capillary numbers. The dashed lines are to guide the eye.

as the pressure-driven drainage is no longer strong enough (figure 13*d–f*), and fluid is pumped back into the film until a final stationary situation is established. Although the stationary end value seems to be predicted quite accurately with asymptotic theories, the history of the film profile is complex and not described by any of those theories.

The capillary numbers investigated here, where the stationary state is an issue, are relatively large. The theory predicts that drainage will always be halted. Recently, Baldessari & Leal (2005) found with a small-capillary-number asymptotic analysis for touching spherical drops, based on solving Stokes flow in tangent sphere coordinates, that the strength of the internal circulation scales as Ca and the velocity of the outflow as $Ca^{1/2}$ (Baldessari & Leal 2005), meaning that in the limit of $Ca \to 0$, the internal circulation no longer plays a role. However, from the continuity equation for the fluid in the film:

$$\dot{h}r^2 \sim u_r h r, \tag{4.2}$$

we find, with $r \sim a$, $a \sim RCa^{1/2}$, and h decaying algebraically in time:

$$u_r \sim RCa^{1/2} t^{-1}. \tag{4.3}$$

So the radial outflow velocity will become smaller than the velocity associated with the internal circulation, which is independent of time and film thickness, and thus the internal circulation eventually will always be important, even for small capillary numbers. However, with the cubic dependence of the stationary film thickness on the capillary number, one could question the relevance of the length scales involved for capillary numbers approaching 0.

For low capillary numbers, for which no stationary profile has been established yet, we find the film to drain as $h_{min} \sim t^{-4/5}$, see figure 14, similar to the long-term asymptote for the buoyancy-driven case. This drainage rate, however, is only valid in an intermediate regime, since eventually the internal circulation will take over and form a steady-state situation, which can be seen in figure 14 for $Ca = 0.005$, where the evolution of the minimum film thickness is diverting from the asymptote. But even for the regime in which we find asymptotic drainage, the absolute value does not correspond well with the analytical solution for the buoyancy-driven cases. As

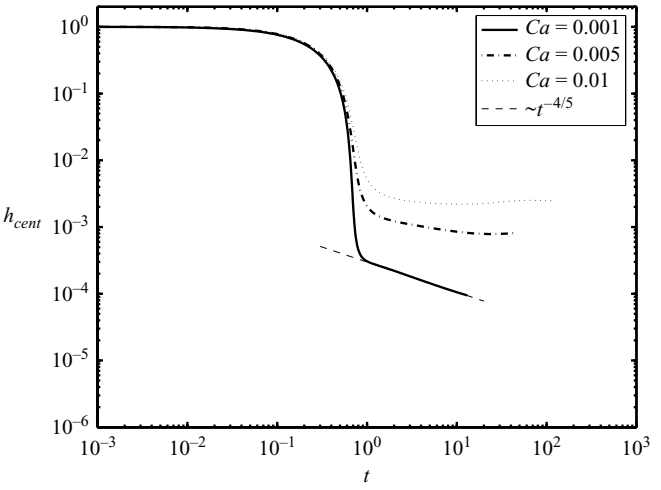

FIGURE 15. Film thickness at the centreline over time for multiple capillary numbers. The dashed line is to guide the eye.

the drainage rate diverges from the asymptote, the film starts to drain at a faster rate. This is a trend similar to what we find for all the lower capillary numbers ($Ca < 0.04$): the drainage rate increases before the minimal film thickness is obtained, as can be seen in figure 14 for $Ca = 0.01$.

For the evolution of h_{cent}, plotted in figure 15, we find asymptotic drainage only for $Ca = 0.001$. For higher capillary numbers, the development of stationary profiles becomes significant already early in the drainage process. For $Ca = 0.001$, where the internal circulation is considered not to be important and the collision is thought to be similar to a buoyancy-driven one, we find h_{cent} not to scale as $\sim t^{-3/5}$, as for the buoyancy-driven case, but to an asymptote that is apparently equal to $\sim t^{-0.45}$. This shows that an external-flow-driven collision is not fully identical to a buoyancy-driven one, even for small capillary numbers, where the development of a stationary film profile is not (yet) an issue, although they appear to be similar.

4.3. *Van der Waals forces*

If van der Waals forces are included, it is important to specify at which interfacial distance they become dominant. This distance is called the critical film thickness h_{crit}. Here the definition as suggested by Chesters (1991) is used, and is illustrated in figure 16.

The strength of the van der Waals forces, expressed by the dimensionless Hamaker parameter A, is varied for a large number of capillary numbers (choices for A and Ca are motivated in § 4.4). Our results show a weak dependence of h_{crit} on the capillary number. Instead of proposing a new relationship between A and h_{crit}, we compare our data with published literature, in particular the work of Chesters & Bazhlekov (2000). For the film radius in the thin-film scaling we used the small-deformation theory estimate. It is observed that high values of A can lead to so-called nose rupture, where coalescence can occur before a film develops (see e.g. figure 23).

Two relations between $\overline{h}_{crit}$ and $\overline{A}$ are given in figure 17: one derived by Chesters (1991) obtained from a force balance yielding $2\overline{h}_{crit} = (\overline{A}/2)^{1/3}$ and the second an empirical relation proposed by Chesters & Bazhlekov (2000), based on data collected with their thin-film description: $2\overline{h}_{crit} = \frac{2}{3}\overline{A}^{0.3}$ (the factor 2 in front of $\overline{h}$ is to compensate

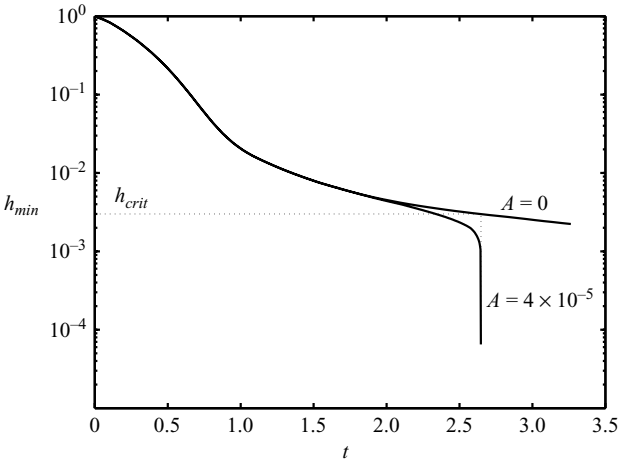

FIGURE 16. Minimal film thickness in time for $Ca = 0.025$ in the absence of van der Waals forces ($A = 0$) and with van der Waals forces included ($A = 4.10^{-5}$). The dotted line represents the definition of the critical film thickness according to Chesters (1991).

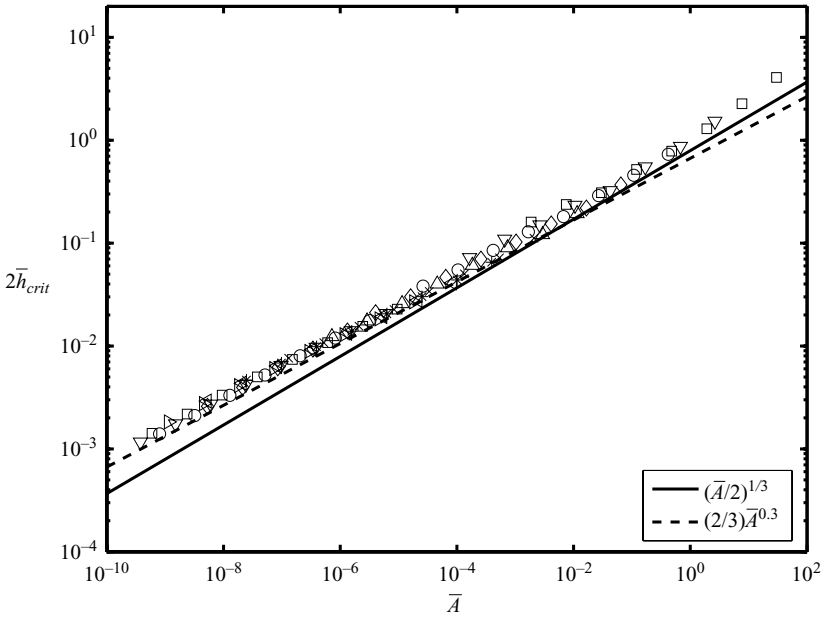

FIGURE 17. Critical film thickness as function of dimensionless Hamaker parameter with the data converted to the scaling of Chesters & Bazhlekov (2000). The symbols represent the results from our simulations from various values of A and Ca (see figure 22); the lines are two different relations from Chesters (1991) and Chesters & Bazhlekov (2000) (see text).

for a difference in scaling definition). In figure 17 it is observed that the empirical relationship gives a better description at lower values of $\overline{A}$, which was also reported by Chesters & Bazhlekov (2000), while the scaling based on the force balance applies at high values of $\overline{A}$. Not only do the slopes of the data correspond with the relations, but, strikingly, also the absolute values. Apparently the type of collision, or the magnitude of the velocity outside the film, does not influence the film thickness at

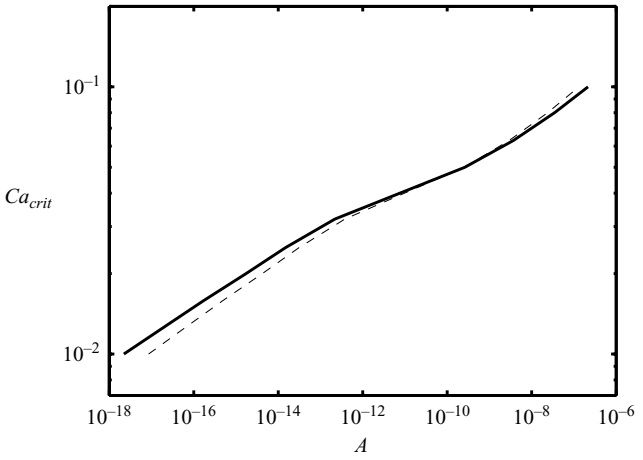

FIGURE 18. The critical capillary number (above which coalescence is prevented) as function of the Hamaker parameter. The solid line is based on $\overline{h}_{crit} = (2/3)\overline{A}^{0.3}$ and the dashed line on $\tilde{A}_{crit} = 1.49$ (see Nemer *et al.* 2004).

which van der Waals forces become dominant, since the simulations by Chesters & Bazhlekov (2000) were conducted in a constant approach case, and ours in an external-flow-driven collision. Therefore, it will often be sufficient to track only the evolution of the minimal film thickness in time in the absence of van der Waals forces to determine at which point film rupture will occur.

The definition of Chesters (1991) of the critical film thickness shows an influence of the rate of thinning $\mathrm{d}h/\mathrm{d}t$ at the moment of rupture for $A = 0$. This is the reason why the data at high values of $\overline{A}$ give the largest deviation from the results of Chesters & Bazhlekov (2000) since they represent a combination of high A and low Ca; consequently $\mathrm{d}h/\mathrm{d}t$ is large and determining the critical film thickness under these conditions is sensitive to small deviations. The same argument explains the dependence of h_{crit} on the capillary number, and combining the $Ca^{1/2}$ scaling of the film radius with equation (2.17) yields $h_{crit} \sim Ca^{0.1}$.

If the critical film thickness is lower than the stationary film thickness or, better, lower than the minimum h_{min} obtained in time, no coalescence will occur. Thus a critical capillary number Ca_{crit} can be defined above which coalescence is prevented. The data for the minimal film thickness in time (see figure 11) were converted to a dimensionless Hamaker parameter that would correspond to that critical film thickness. We have used the scaling relationship $\overline{h}_{crit} = \frac{2}{3}\overline{A}^{0.3}$ in combination with $a = 2.086Ca^{1/2}$ to find the solid line in figure 18. Nemer *et al.* (2004) found a critical Hamaker parameter of $\tilde{A}_{crit} = 1.49$, where

$$\tilde{A} = 3\pi^2 \frac{A}{h_{min}^3} \tag{4.4}$$

in our variables, and we used this result to estimate a critical capillary number, with h_{min} once again based on our simulations (figure 18, dashed line). As one can see, there are only minor differences between the two approaches to Ca_{crit}. The critical capillary number proves to be only weakly dependent on the dimensionless Hamaker parameter (combining $h_{crit} \sim A^{1/3}$ and $h_{min,stat} \sim Ca^3$ yields $Ca_{crit} \sim A^{1/9}$). So for head-on collisions a critical capillary number is only an issue for large drops at large

capillary number. Notice that the origin of the existence of a critical capillary number is different for head-on collisions, where it is governed by a stationary state, compared to glancing collisions where there is a finite contact time.

4.4. *Drainage time*

Finally, we studied head-on collisions between drops with clean interfaces and compared the drainage time with recent experimental results obtained with a four-roll mill (Yang *et al.* 2001; Leal 2004). Two drops are placed at a mass-centre distance of $4R$. The four-roll mill generates a planar flow but since the drops are small, an axisymmetric bi-extensional flow will not be too different. No results were reported for $\lambda = 1$, but similar trends were observed for viscosity ratios ranging from about 10^{-1} to 10 (Yoon *et al.* 2005).

The drainage time is defined as the time from when δ equals $2R$ (the minimum film thickness at this moment is called h_0) to the moment of film rupture. In the experimental data the scaled drainage time was found to be proportional to $Ca^{3/2}$ for higher capillary numbers $3.10^{-3} < Ca < 3.10^{-2}$, but seemingly reached a plateau at lower values for Ca.

Based on their reported values for H ($3.166.10 \times 10^{-21}$ J) and σ (4.2×10^{-3} Nm^{-1}), we find $A = 4 \times 10^{-12}$ for a drop of 100 μm radius, which is the upper limit of drop radii investigated. The simulation results are shown in figure 19. It is observed that the drainage time indeed scales with $Ca^{3/2}$ in approximately the same range of capillary numbers, except for high capillary numbers where the slope seems to decrease. This effect can be ascribed to the strength of the internal flow, as discussed above, where the drainage rate increases prior to the development of a stationary film profile. However, at lower capillary numbers the drainage time seems to scale with Ca^1, instead of becoming constant, as was found in the experiments.

One other observation is that for the lower capillary numbers there is incomplete film formation, as shown in figure 20. Instead of following a $Ca^{1/2}$ scaling, the film radius at rupture is lower, indicating a transition to nose rupture instead of rim rupture. Moreover, we find the starting film thickness h_0, taken as $\delta = 2R$, to scale as $\sim Ca^{0.8}$ over almost the full range of capillary numbers studied (figure 21). The power maybe a very weak function of the viscosity ratio λ (Baldessari 2004).

Next, we focus on the influence of the drop radius. With the capillary number fixed (the equivalent shear rate G is thus inversely proportional to the drop radius), the only parameter left to influence the radius is the dimensionless Hamaker parameter A. Simulations for multiple values of A (or R) were conducted and the results for the drainage time are presented in figure 22 (based on the same values for H and σ as used for the 100 μm radius drop, these results correspond to drop radii varying from 6.25 to 800 μm). The drainage time increases with decreasing A, since the critical film thickness is lower. Furthermore, we find similar trends: at low capillary numbers the drainage time scales as Ca^1 and at higher capillary number as $Ca^{3/2}$. However, the capillary number at which the transition between the two scalings takes place changes and shifts to the right for increasing A (or decreasing R). For combinations of high capillary numbers and low A, the slope decreases at high Ca and for some combinations we even observed no film rupture at all, but a steady situation due to the strength of the internal flow ($Ca > Ca_{crit}$). No drainage time was defined for these situations. The film radius at rupture decreases with increasing A, figure 23, leading to nose rupture for combinations of low Ca and high A.

The experimental data on drainage collected by Yang *et al.* (2001) (in the range where the drainage time scaled as $Ca^{3/2}$) collapsed into a single curve if the

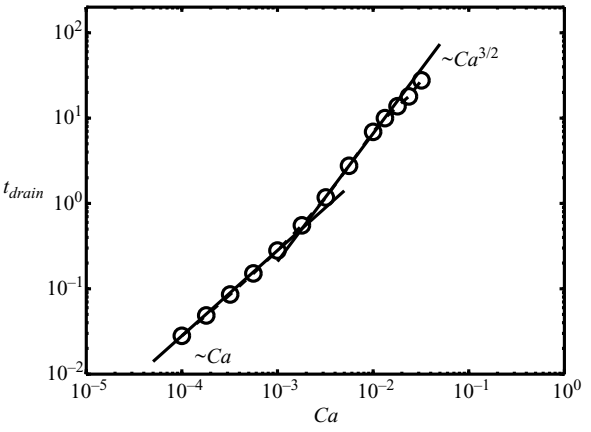

FIGURE 19. Drainage time as function of capillary number for $A = 4 \times 10^{-12}$ (solid lines are to guide the eye).

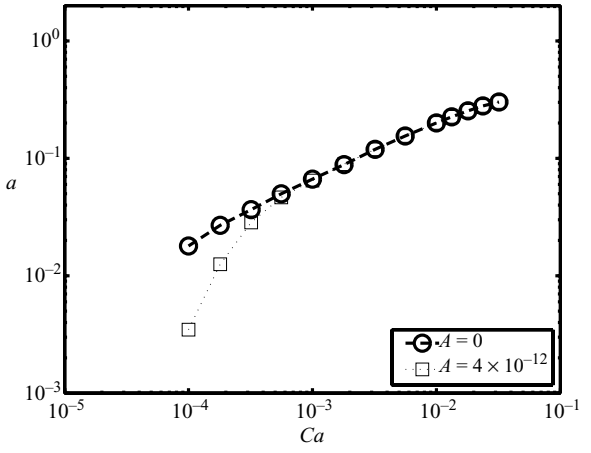

FIGURE 20. Film radius as function of capillary number with and without van der Waals forces included. For the case with van der Waals forces the film radius is taken as the radius at the moment of rupture.

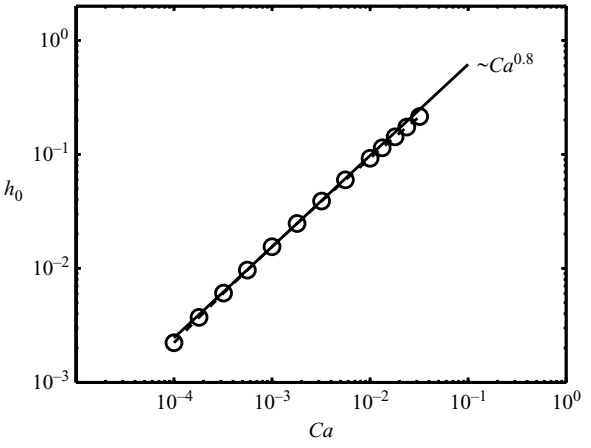

FIGURE 21. Film thickness as function of capillary number at the moment $\delta = 2R$. The solid line is to guide the eye.

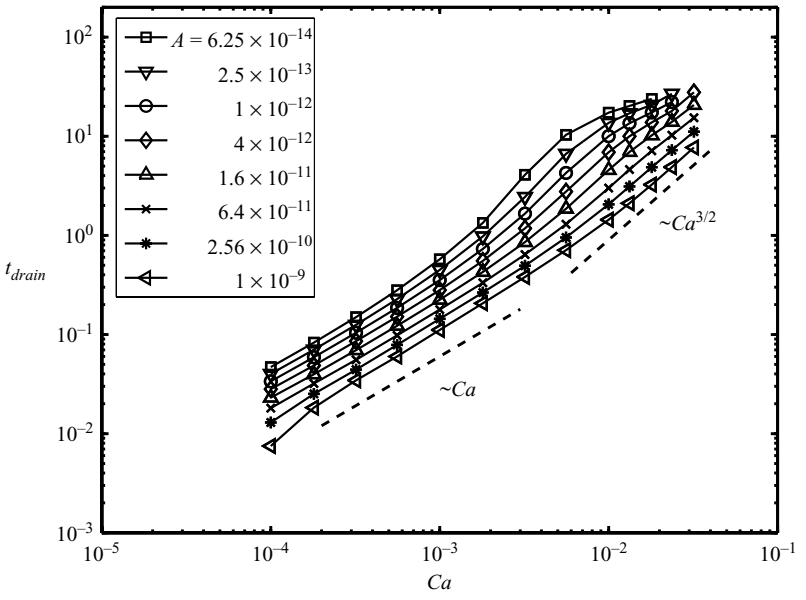

FIGURE 22. Drainage time as function of capillary number for multiple values of A. The dashed lines are to guide the eye.

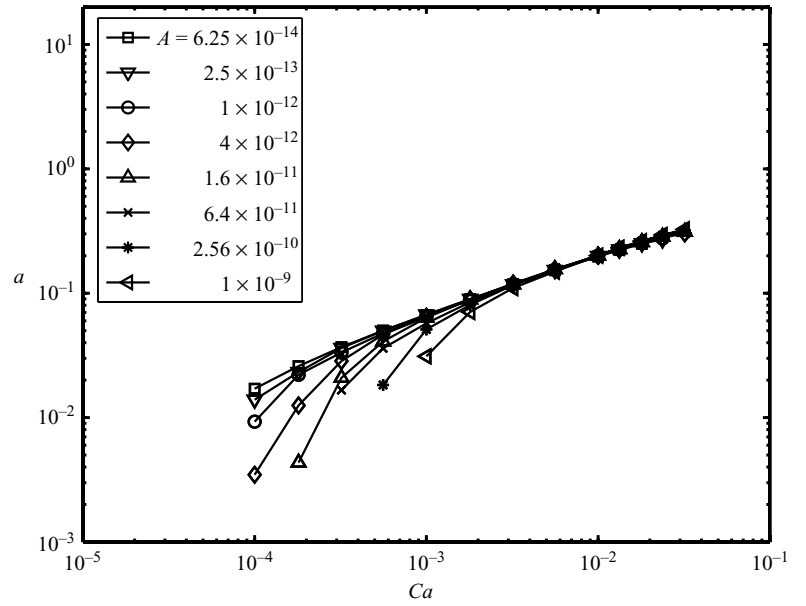

FIGURE 23. Film radius at the moment of rupture as function of the capillary number for multiple values of A.

dimensionless drainage time is scaled with $R^{-5/4}$. Our data do not match this relationship. Also, since the capillary number at which the transition in power-law dependence takes place changes for different drop radii, a simple shift along the vertical axis cannot yield a master curve for the complete range of capillary numbers. We find, by fitting our simulation data, that the drainage time scales with $A^{-0.15}$

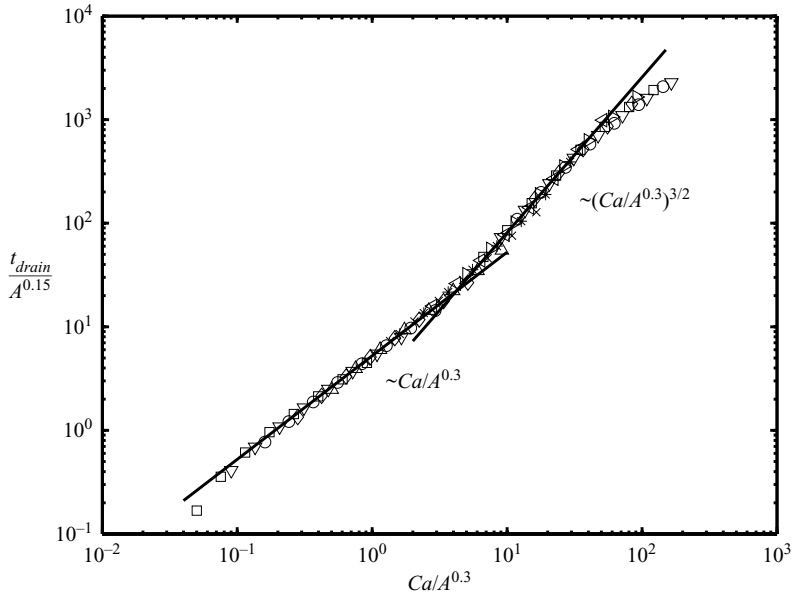

FIGURE 24. Scaled drainage time as a function of scaled capillary number. The symbols correspond with the legend of figure 22. The solid lines are to guide the eye.

(or $R^{0.3}$) and the capillary number with $A^{-0.3}$ (or $R^{0.6}$) to obtain a master curve, see figure 24. This new scaling, however, is not in disagreement with a simple drainage model, as will be clarified below.

We support the explanation for the change in slope of drainage time versus Ca at low capillary numbers given by Yang *et al.* (i.e. the transition from coalescence between two touching drops with a fully developed film formed between them, to coalescence between spherical drops). However, we interpret the drainage model in a different way, which not only explains the Ca scaling, but also the drop radius scaling, and yields a Ca^1 scaling at lower capillary numbers, instead of a constant value. For that we consider the simple drainage model for partially mobile interfaces (which corresponds to moderate viscosity ratios), as suggested by Chesters (1991):

$$-\frac{\mathrm{d}h}{\mathrm{d}t} \sim \frac{2(2\pi\sigma/R)^{3/2}h^2}{\pi\mu_d F^{1/2}}. \tag{4.5}$$

In the case of a fully developed film the contact force F can be estimated from the lubrication pressure in the film:

$$F \approx 2\pi \int_0^a \Delta p r \,\mathrm{d}r \approx \pi a^2 \frac{\sigma}{R}, \tag{4.6}$$

if we assume $\Delta p \approx \sigma/R$.

Substituting equation (4.6) into (4.5) and rearranging, we find

$$-\lambda a Ca \frac{\mathrm{d}h}{h^2} \sim G\,\mathrm{d}t, \tag{4.7}$$

which basically is equation (19) from Yang *et al.*

For a fully developed film we find the film radius by equating the contact force to the Stokes drag force acting upon the drops:

$$F \approx 6\pi\mu_0 G R^2, \tag{4.8}$$

and thus

$$a \sim RCa^{1/2}, \tag{4.9}$$

which is consistent with our simulations (see figure 8). Substituting equation (4.9) into (4.7), and integrating from h_0 to h_{crit} results in

$$t_{drain}G \sim \lambda Ca^{3/2}\frac{R}{h_{crit}}, \tag{4.10}$$

under the assumption that $h_{crit} \ll h_0$. This result is identical to that found by Yang *et al.*

If we now substitute $h_{crit}/R \sim A^{0.3}$ (which is a good approximation, as can be seen in figure 17) into (4.10), and shift the term $A^{0.15}$ to the left-hand side, we find

$$t_{drain}GA^{-0.15} \sim \lambda(CaA^{-0.3})^{3/2}. \tag{4.11}$$

On the other hand if the drops are spherical, we estimate the contact force in the drainage stage to be comparable to the van der Waals forces acting on spherical drops in near-contact motion $F_{vdw} \sim HR/h^2$ (Hamaker 1937), which, if substituted into equation (4.5), yields after rearranging

$$-\lambda R^2 A^{1/2} Ca\frac{\mathrm{d}h}{h^3} \sim G\,\mathrm{d}t. \tag{4.12}$$

Integrating this equation results in

$$t_{drain}G \sim \lambda A^{1/2} Ca\left(\frac{R}{h_{crit}}\right)^2. \tag{4.13}$$

As for the fully developed film, we find

$$t_{drain}GA^{-0.15} \sim \lambda CaA^{-0.25}, \tag{4.14}$$

for $h_{crit}/R \sim A^{0.3}$, and

$$t_{drain}GA^{-0.15} \sim \lambda CaA^{-0.32}, \tag{4.15}$$

for $h_{crit}/R \sim A^{1/3}$. This latter estimate seems a better scaling, since spherical drops correspond to high values of $\overline{A}$.

Surprisingly, we can also find the same scaling if we estimate the film radius for spherical drops from

$$\left(\frac{a}{R}\right)^2 \approx \frac{h}{R}. \tag{4.16}$$

Substituting equation (4.16) into equation (4.7), integrating and rearranging yields:

$$t_{drain}GA^{-0.15} \sim \lambda CaA^{-0.3} \tag{4.17}$$

for $h_{crit}/R \sim A^{0.3}$. This, however, requires the assumption that the pressure in the film for spherical drops is comparable to the capillary pressure σ/R (as it would be in a fully developed film), but it is generally assumed to be much lower.

As can be seen in figure 24, plotting $t_{drain}GA^{-0.15}$ as function of $CaA^{-0.3}$ seems to capture both regimes quite well, yielding one master curve. It is surprising that this drainage model gives an accurate scaling relationship for the drainage time, despite

its simplicity. (The model also predicts a drainage rate ($h \sim t^{-1}$) but this rate is not in agreement with our simulations (figure 14)). Another way to predict the drainage time, is to equate to the van der Waals stresses at the moment of rupture to the capillary stresses:

$$H/h_{min,crit}^3 \sim \sigma/R, \tag{4.18}$$

or

$$\overline{h}_{min,crit} \sim Ca^{-1}A^{1/3}, \tag{4.19}$$

and with a drainage rate of $\overline{h} \sim \overline{t}^{-4/5}$, we find

$$Gt_{drain} \sim Ca^{7/4}A^{-5/12}. \tag{4.20}$$

In figure 22 one can see that for $A = 6.25 \times 10^{-14}$ around $Ca = 3 \times 10^{-3}$ the drainage time indeed seems to scale more strongly than $Ca^{3/2}$. But the regime of drainage where this could be the case is very limited. The capillary number should be small enough that the $h \sim t^{-4/5}$ drainage behaviour can be established, and A should be small enough that rupture will not occur before this asymptote is reached but not so small that the internal circulation affects the film drainage ($Ca < Ca_{crit}$). Equation (4.20) can be rewritten as

$$Gt_{drain}A^{-0.15} \sim (CaA^{-0.32})^{7/4}. \tag{4.21}$$

This scaling is not observed in figure 24, since there is only a limited range of combinations of Ca and A in which it is found.

There is a difference between the Ca^1 scaling we find at lower capillary numbers, and the plateau value found in experiments, where the drainage time was apparently not only independent of the capillary number, but also independent of the drop radius. There might be physical reasons to explain a plateau at lower capillary numbers (Baldessari 2004), but we also found that at low capillary numbers the drainage time is very sensitive to accurately determining the starting time when $\delta = 2R$. Our simulations even required accurate interpolation between two nodes when calculating the location of the mass centres, a resolution that might not be reached with the optical microscope used in the experiments ($\approx 1\,\mu$m/pixel). Furthermore, a constant drainage time cannot hold in the limit of $Ca \to 0$, as eventually h_{crit} becomes larger than h_0 and the drainage time would be zero (or even negative) for a non-zero capillary number.

Our scaling leaves us with the question of why $CaA^{-0.3}$ is the independent variable, or, in other words, why do we have to include a dependence on drop radius in both the drainage time and the (rescaled) capillary number. Currently we do not have an answer to this question.

Finally, by equating the drainage rate to the external approach velocity, RG, one can estimate h_0, although the definition is not similar to the one used above. This yields for the partially mobile case in combination with equation (4.8)

$$h_0 \sim RCa^{3/4}. \tag{4.22}$$

The $Ca^{0.8}$ scaling we find here (figure 21) is not different.

5. Conclusions

We simulated head-on collisions of viscous drops with the same viscosity as the matrix fluid using a non-singular boundary integral method. A contour-integral representation for the single-layer potential proved to have sufficient stability and

accuracy to simulate film drainage where the film thickness was 10^{-4} times smaller than the undeformed drop radius, capturing both the inner and the outer problem of drop coalescence. With this method various results from asymptotic theories could be reproduced, but in most cases we only found a match in a limited range of parameters. The constant-approach-force case, as often simulated with thin-film descriptions, corresponds to a buoyancy-driven collision. The long-term asymptotic drainage behaviour found is similar to a recently derived analytical solution, and not the previously assumed drainage rate based on a scaling argument. External-flow-driven collisions also yield this long-term drainage behaviour, but only for low capillary numbers, and before the drainage is halted altogether. For the centreline thickness, the film drainage was different than for buoyancy-driven collisions. This means that buoyancy-driven collisions are fundamentally different from external-flow-driven collisions, as has been recently shown. Also if van der Waals forces are included we obtain good correspondence with asymptotic theories, when investigating the critical film thickness as a function of the Hamaker parameter. Finally, the time to drain the film for head-on collisions is investigated as a function of the capillary number and the drop radius. In an empirical way a rather unusual scaling relation is found that is not in disagreement with a simple drainage theory: the independent variable is, however, $CaA^{-0.3}$ and not the capillary number itself. Furthermore there is a transition in the power-law dependence from 1 to 1.5, corresponding to a transition from a collision between spherical drops to film drainage in a fully developed film.

The authors acknowledge the Dutch Polymer Institute (DPI) for financing this project (#446), Dr I. B. Bazhlekov for help and support and Professor M. Loewenberg for detailed commentary on the manuscript.

REFERENCES

Abid, S. & Chesters, A. 1994 The drainage and rupture of partially-mobile film between colliding drops at constant velocity approach. *Intl J. Multiphase Flow* **20**, 613.

Abramowitz, M. & Stegun, I. 1965 *Handbook of Mathematical Functions with Formulas, Graphs, and Mathematical Tables*. Dover.

Baldessari, F. 2004 Flow-induced coalescence of drops: Theory and simulation. PhD thesis, University of California, Santa Barbara.

Baldessari, F. & Leal, L. 2005 Two touching spherical drops in a uniaxial extensional flow: Analytic solution to the creeping flow problem. *J. Colloid Interface Sci.* **289**, 262.

Bazhlekov, I., Anderson, P. & Meijer, H. 2004 Non-singular boundary-integral method for deformable drops in viscous flows. *Phys. Fluids* **16**, 1064.

Bazhlekov, I., Chesters, A. & van de Vosse, F. 2000 The effect of the dispersed to continuous-phase viscosity ratio on film drainage between interacting drops. *Intl J. Multiphase Flow* **26**, 445.

Bazhlekova, E. & Bazhlekov, I. 2003 Contour-integral representation of single and double layer potentials for axisymmetric problems. *Lecture Notes in Computer science* **2542**, 387.

Bladwzdziewicz, J., Wajnryb, E. & Loewenberg, M. 1999 Hydrodynamic interactions and collision efficiencies of spherical drops covered with an incompressible surfactant film. *J. Fluid Mech.* **395**, 29.

Chesters, A. 1991 The modelling of coalescence of fluid-liquid dispersions: a review of current understanding. *Trans. Inst. Chem. Engrs* A **69**, 259.

Chesters, A. & Bazhlekov, I. 2000 Effect of insoluble surfactants on drainage and rupture of a film between drops interacting under a constant force. *J. Colloid Interface Sci.* **230**, 229.

Cristini, V., Blawzdziewicz, J. & Loewenberg, M. 2001 An adaptive mesh algorithm for evolving surfaces: Simulation of drop breakup and coalescence. *J. Comput. Phys.* **168**, 445.

Davis, R. 1999 Buoyancy-driven viscous interaction of a rising drop with a smaller trailing drop. *Phys. Fluids* **11**, 1016.

Hamaker, H. 1937 The London-van der Waals attraction between spherical particles. *Physica* **4**, 1058.

Jones, A. & Wilson, S. 1978 The film drainage problem in drop coalescence. *J. Fluid Mech.* **87**, 263.

Klaseboer, E., Chevaillier, J., Gourdon, C. & Masbernat, O. 2000 Film drainage between colliding drops at constant approach velocity: experiments and modelling. *J. Colloid Interface Sci.* **229**, 274.

Leal, L. 2004 Flow induced coalescence of drops in a viscous fluid. *Phys. Fluids* **16**, 1833.

Li, D. 1994 Coalescence between two small bubbles or drops. *J. Colloid Interface Sci.* **163**, 108.

Loewenberg, M. & Hinch, E. 1996 Numerical simulation of concentrated emulsion in shear flow. *J. Fluid Mech.* **321**, 395.

Nemer, M. 2003 Near-contact motion of liquid drops in emulsions and foams. PhD thesis, Yale University.

Nemer, M., Chen, X., Papadopoulos, D., Blawzdziewicz, J. & Loewenberg, M. 2004 Hindered and enhanced coalescence of drops in Stokes flow. *Phys. Rev. Lett.* **92**, 114501.

Pozrikidis, C. 1992 *Boundary-Integral and Singularity Methods for Linearized Viscous Flow*. Cambridge University Press.

Rallison, J. & Acrivos, A. 1978 A numerical study of the deformation and burst of a viscous drop in an extensional flow. *J. Fluid Mech.* **89**, 191.

Rother, M. & Davis, R. 2001 The effect of slight deformation on droplet coalescence in linear flows. *Phys. Fluids* **13**, 1178.

Rother, M., Zinchenko, A. & Davis, R. 1997 Buoyancy-driven coalescence of slightly deformable drops. *J. Fluid Mech.* **346**, 117.

Stone, H. 1994 Dynamics of drop deformation and breakup in viscous flows. *Annu. Rev. Fluid Mech.* **26**, 65.

Tucker III, C. & Moldenaers, P. 2002 Microstructural evolution in polymer blends. *Annu. Rev. Fluid Mech.* **34**, 177.

Valkovska, D., Danov, K. & Ivanov, I. 2000 Effect of surfactants on the stability of films between two colliding small bubbles. *Colloids Surf.* A **175**, 179.

Yang, H., Park, C., Hu, Y. & Leal, L. 2001 The coalescence of two equal-sized drops in a two-dimensional linear flow. *Phys. Fluids* **13**, 1087.

Yeo, L., Matar, O., de Ortiz, E. & Hewitt, G. 2003 Film drainage between two surfactant-coated drops colliding at constant approach velocity. *J. Colloid Interface Sci.* **257**, 93.

Yiantsios, S. & Davis, R. 1990 On the buoyancy-driven motion of a drop towards a rigid surface or a deformable interface. *J. Fluid Mech.* **217**, 547.

Yiantsios, S. & Davis, R. 1991 Close approach and deformation of two viscous drops due to gravity and van der Waals forces. *J. Colloid Interface Sci.* **144**, 412.

Yoon, Y., Borell, M., Park, C. & Leal, L. 2005 Viscosity ratio effects on the coalescence of two equal-sized drops in a two-dimensional linear flow. *J. Fluid Mech.* **525**, 355.

Zinchenko, A. & Davis, R. 2005 A multipole-accelerated algorithm for close interaction of slightly deformable drops. *J. Comput. Phys.* **207**, 695.

Zinchenko, A., Rother, M. & Davis, R. 1997 A novel boundary-integral algorithm for viscous interaction of deformable drops. *Phys. Fluids* **12**, 484.